International Journal of Extreme Manufacturing

Localized electrodeposition micro additive manufacturing of pure copper microstructures

OPEN ACCESS
IOP Publishing | IMMT
International Journal of Extreme Manufacturing
Int. J. Extrem. Manuf. **4** (2022) 015101 (11pp)
https://doi.org/10.1088/2631-7990/ac3963

Localized electrodeposition micro additive manufacturing of pure copper microstructures

Wanfei Ren, Jinkai Xu*, Zhongxu Lian, Xiaoqing Sun, Zhenming Xu and Huadong Yu*

Ministry of Education Key Laboratory for Cross-Scale Micro and Nano Manufacturing, Changchun University of Science and Technology, Changchun 130022, People's Republic of China

E-mail: xujinkai2000@163.com and yuhuadong@cust.edu.cn

Received 4 May 2021, revised 31 August 2021
Accepted for publication 12 November 2021
Published 25 November 2021

Abstract

The fabrication of pure copper microstructures with submicron resolution has found a host of applications, such as 5G communications and highly sensitive detection. The tiny and complex features of these structures can enhance device performance during high-frequency operation. However, manufacturing pure copper microstructures remain challenging. In this paper, we present localized electrochemical deposition micro additive manufacturing (LECD-μAM). This method combines localized electrochemical deposition (LECD) and closed-loop control of atomic force servo technology, which can effectively print helical springs and hollow tubes. We further demonstrate an overall model based on pulsed microfluidics from a hollow cantilever LECD process and closed-loop control of an atomic force servo. The printing state of the micro-helical springs can be assessed by simultaneously detecting the *Z*-axis displacement and the deflection of the atomic force probe cantilever. The results showed that it took 361 s to print a helical spring with a wire length of 320.11 μm at a deposition rate of 0.887 μm s^{-1}, which can be changed on the fly by simply tuning the extrusion pressure and the applied voltage. Moreover, the *in situ* nanoindenter was used to measure the compressive mechanical properties of the helical spring. The shear modulus of the helical spring material was about 60.8 GPa, much higher than that of bulk copper (~44.2 GPa). Additionally, the microscopic morphology and chemical composition of the spring were characterized. These results delineate a new way of fabricating terahertz transmitter components and micro-helical antennas with LECD-μAM technology.

Supplementary material for this article is available online

Keywords: rapid prototyping, localized electrochemical deposition, additive manufacturing, mechanical properties, micro-helical spring

* Authors to whom any correspondence should be addressed.

2631-7990/22/015101+11$33.00

1. Introduction

The rapid application of pure copper microstructures and devices in the field of 5G communications and highly sensitive detections serves as a driving force for the continuous development of related micromanufacturing technologies. Microstructures have played an irreplaceable role in signal and data transmission between electrical devices and device units. In the last two decades, major efforts have resulted in superior microstructure manufacturing capabilities. Recently, two important frontiers of microstructure manufacturing include the integration of microfabrication and micro additive manufacturing (μAM). In microfabrication, although both focused ion beams and electron beam lithography have very high micromachining resolutions, these methods usually have expensive and difficult-to-upgrade steps [1]. A technology combining the two methods of micro-milling and micro electrical discharge machining has been proposed for manufacturing micro-cavity arrays [2]. This technique can achieve a size feature of a few hundred microns. It is technically difficult to apply this technique to micron or even sub-micron accuracy. In μAM, ultraviolet-assisted direct writing technology was utilized to generate a three-dimensional (3D) independent helical spring-shaped as a strain sensor [3, 4], but this technology is limited to manufacturing non-metallic structures. In comparison, direct ink writing (DIW) has overcome the challenge of manufacturing metal structures, such as 3D electronic and optoelectronic microstructures, and it has proven to be a useful approach in manufacturing freestanding spiral architectures on flexible and rigid substrates at the scale of tens of micron by further combining laser and DIW technologies [5, 6]. However, such methods remain limited in fabricating pure metal structures. Additionally, although laser-induced forward transfer and chemical etching for pure metal have been proven to be effective methods [7], the processing quality requires further improvement. Atomic layer deposition can generate microstructures, but the constraints of reactants and deposition conditions limit its use for a wide range of applications [8, 9]. Additionally, focused ion beam induced deposition has been used to grow a 105 nm diameter carbon spring and a 25 nm thick gold layer deposited on an outer surface. The spring was used to transfer the direction of wave propagation [10]. However, this process cannot achieve the one-step metallization manufacturing of micro-springs.

Electrochemical deposition is a cost-effective and environment-efficient technology that can provide an alternative and powerful method of fabricating 3D microstructures [11–15]. The use of the micro electroforming process has important applications in manufacturing microfluidic chip molds, but this electrochemical deposition method still depends on a mask [16]. In terms of localized deposition, two major efforts have been focused on localization abilities, which can improve manufacturing resolution significantly. One effort involves continuously reducing the cross-sectional area of the fine metal anode in localized electrochemical deposition (LECD) [17, 18]. Another effort involves setting an ultra-fine hollow glass tube as a mass transfer pipette in meniscus confined electrochemical deposition (MCED) [19–21]. To improve the printing capabilities of 3D structures, an asymmetric anode or a five-axis motion platform must be attached to ordinary LECD technology [22], but this step is cumbersome and has costly upgrades. Although MCED technology can print high-resolution independent 3D tiny coil springs [23], ultra-low printing speed and manufacturing based on a linear structure limits the large-scale promotion of this technology.

However, people have not yet seen AM technology fully demonstrate its potential for fabricating pure copper metal structures. As one new frontier of advanced electrodeposition technology, LECD-μAM, which can effectively print pure copper microstructure, is the integration of LECD and the closed-loop control of an atomic force servo. In this technology, a hollow atomic force probe (AFP) with mature technology applications in the biological and cellular fields is introduced as a liquid mass transfer tool (named FluidFM) [24–26], achieving a breakthrough in localized mass transfer. This technology is based on FluidFM and LECD as LECD-μAM. FluidFM plays two important roles in LECD-μAM. One role is to successfully detect the formation of sub-micron voxels as a force sensor. Furthermore, adjusting the position of the probe tip and changing the probe's bending shape solves the problem of high-quality combination between sub-micron voxels. FluidFM also acts as an electrolyte mass transfer pipette [27–29]. This role involves pumping due to the extrusion pressure at the end of the AFP cantilever, which solves the problem of high local mass transfer in the micro area. These two roles guarantee the maskless manufacturing of tiny pure copper structures with sub-micron resolution. Compared with microfabrication technology, the LECD-μAM operation process does not require high-energy particle beams, vacuum, an inert gas environment, or post-processing operations to manufacture pure copper microstructure. Compared with electrodeposition technology, the LECD-μAM operation process does not require a mask, it is more environmentally friendly (copper sulfate solution 0.7 μl), and possesses significantly improved localization. There is no need to control the humidity of the external environment, and there is no need to control the probe retreat speed, ensuring high-quality integration between voxels. These advantages provide a broad application space for LECD-μAM in microstructure manufacturing.

2. Experiment setup

As shown in figure 1(a), the entire printing system consisted of four parts: The AFP system, extrusion pressure control system, electrolytic cell system, and *X*/*Y*/*Z* microscale moving system. There were three key technologies applied in this system: (a) closed-loop control system of the atomic force servo, (b) micro-liquid flow, and (c) LECD. A hollow AFP was used to form an electrolyte channel and an extrusion pressure control system was arranged at the end of the cantilever of the AFP to precisely control the extrusion pressure of the electrolyte. The position sensitive detector was used to monitor the deflection of the AFP in order to determine in real-time whether the tip of the AFP perceived successful deposition. The electrolytic

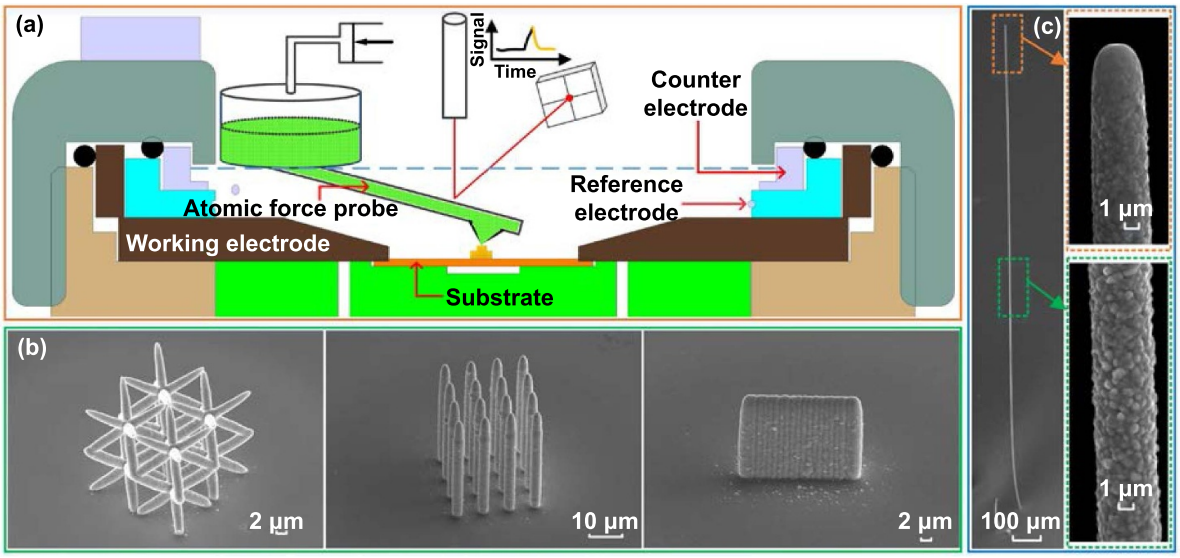

Figure 1. Scheme of the LECD-μAM. (a) The three electrodes system in the electrolytic cell. (b) The lattice monomer, pillar array and a thin wall. (c) A high aspect ratio (about 500) wire.

cell included a working electrode (WE), a counter electrode (CE) and a reference electrode (RE), and all of the electrodes were connected to the potentiostat. The substrate was attached to the WE. The CE was a graphite electrode with excellent conductivity that encircled the electrolytic cell. An Ag/AgCl electrode was used as the RE. Insulation was achieved by placing a Teflon bracket between any electrodes. The *X*/*Y*/*Z* three-axis movement direction was precisely controlled by a precision servo motor. The minimum positioning accuracy of the *X*/*Y* two directions was 500 nm, and the minimum positioning accuracy of the *Z* direction was 10 nm, which was guaranteed by the dual control of the servo motor and the piezoelectric ceramic. Additionally, a numerical model was formed with 3D software, and 3D slice software was used to convert the 3D structure into a data point cloud file. Then, the point cloud data was exported into a (.csv) file and delivered to the printing system. Figure 1(b) displays three different structures including a lattice monomer, pillar array, and thin wall. A high aspect ratio (about 500) wire was printed, as shown in figure 1(c).

The parameters used in this experiment are listed in table 1. For the electrolyte parameters, a $CuSO_4$ solution (0.5 M) was used for the LECD-μAM. The supporting solution was mixed with an H_2SO_4 solution (54 mM) and an HCl solution (0.5 mM). The support solution played an important role as the flexible support and increased the conductivity of the solution. For the fabrication parameters, about −0.5 V was applied to the substrate, and the AFP approaching threshold was set to 0.4 V. The approaching voltage was the voltage threshold of an AFP sensing substrate or a deposited voxel. This voltage threshold represented the degree of deformation of the cantilever of the AFP when the piezoelectric ceramic was triggered to drive the AFP. Simultaneously the extrusion pressure was changed from 20 mbar to 120 mbar 'on the fly' and the interelectrode gap was set to 0.5 μm.

Table 1. The parameters used in this experiment.

Parameter	Value
Copper ion solution	$CuSO_4$ (0.5 M)
Supporting solution	H_2SO_4 (54 mM); HCl (0.5 mM)
Substrate voltage: *E* (V)	−0.46 to −0.56
Approaching voltage (V)	0.4
Extrusion pressure: *P* (mbar)	20–120
Interelectrode gap: (μm)	0.5

2.1. Establishment of the model

Establishing a model for the LECD-μAM involved the closed-loop control theory, fluid flow theory of microfluidic system, and electro-deposition theory. In fact, among the three theories, the atomic force servo was the core link of the entire system. For the first section, microliquid flow, driven by the pulse extrusion pressure, the active electrolyte was replenished in a localized manner because the electrolyte was sprayed from the storage tank along the internal channel of the AFP to be deposited in the micro area. For the second section, electrochemical deposition, all fundamental kinetics parameters of ion movement in the material flux were obtained through electrochemical experiments. For the third section, the closed-loop control system of the atomic force servo as well as the mass and volume of the cantilever of the AFP were significantly greater than those of the tip of the AFP, so the mechanical property of the AFP depended on the cantilever instead of the tip, which merely served as a point of action for the cantilever. The cantilever of the AFP was a force-feedback device that measured the successful growth of metal deposits, and its hollow channel provided an opportunity to achieve electrolyte booster injection technology as a channel of the microfluidic system. The mechanism of action is described in more detail in supporting information, section 1 (available online at stacks.iop.org/IJEM/4/015101/mmedia).

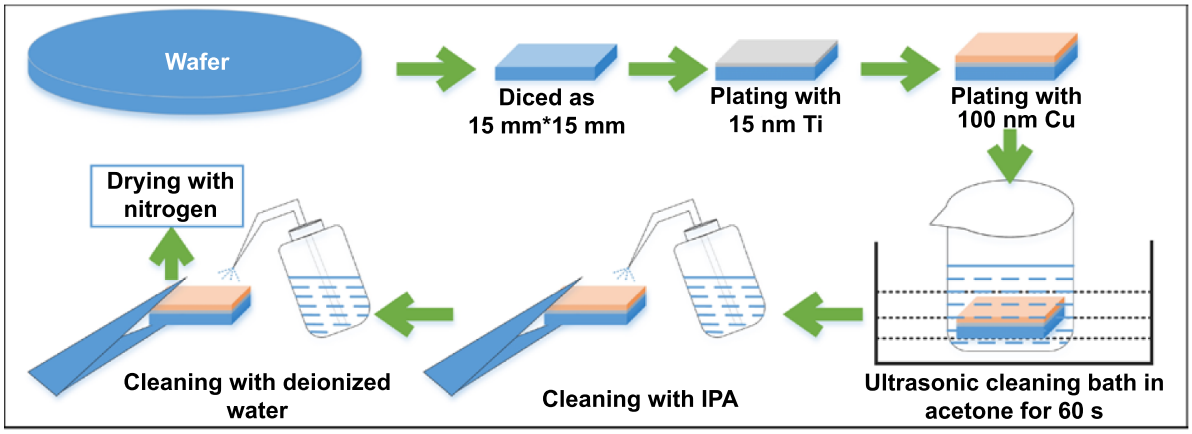

Figure 2. Flow of the substrate preparation.

2.2. Substrate preparation

A wafer with a thickness of 0.5 mm was selected as the substrate. It was cut into 15 × 15 mm squares with a diamond dicing machine. One of the sides was selected to plate a 15 nm titanium layer and then a 100 nm copper layer. The prepared substrate was placed in an acetone solution for ultrasonic cleaning for 60 s. And then the substrate was rinsed with isopropanol and deionized water to remove organic and inorganic impurities. Nitrogen stream was used to dry the rinsed substrate. This preparation flow is shown in figure 2.

2.3. Characterizations

The dimensions of the AFP are displayed in figure S3 (supporting information, section 2). The length of the microcantilever was 200 μm, the width was 40 μm, and the opening diameter of the pyramid-shaped tip was 300 nm. In order to better understand the printed structures fabricated by LECD-μAM, the following advanced instruments were used to further characterize the performance of the structures. Scanning electron microscope (SEM) was used to characterize the morphology of the 3D structures (Zeiss, EVO 20, Germany). Height detail was captured by a laser scanning confocal microscope (ZEISS, LSM700, Germany). Furthermore, a quantitative analysis of the chemical elements was conducted using a field emission electron probe microanalyzer with x-ray spectrometer (JEOL, JXA-8530F Plus, Japan) with a high wavelength resolution. The *in-situ* nanoindenter (Alemnis, Indenter, Switzerland) installed in the high resolution field emission SEM (TESCAN, MAIA3 XMU, Czech Republic) was used to characterize the mechanical properties of the printed micro-helical springs.

3. Results and discussion

3.1. Printing rate and structures performance analysis

In this work, the deposition rate of the microstructures, the shape of the deposits and the morphology of the large-area structures were analyzed. The deposition parameters corresponding to the deposition rate research process are shown in table 2.

Table 2. Deposition parameters of helical spring structure.

Parameter	Value
Helical spring structure diameter: D (μm)	20
Helical spring structure height: H (μm)	50
Helical spring structure pitch: s_1 (μm)	10
Number of coils: n (No.)	5
Helical spring wire diameter: d (μm)	2
Mean time for single voxel (ms)	553
Extrusion pressure P (mbar)	60
Deposition voltage: E (V)	−0.55
Total print time (s)	361
Total voxels (No.)	637

The LECD-μAM simultaneously monitored the coordinate position of the Z-axis probe and the deflection of the AFP cantilever. The deposition process data for the entire cycle of a structure were recorded through real-time data processing. We took a five-turn spiral spring as an example. The parameters such as the diameter, height, pitch, and the wire diameter of the printed helical spring are listed in table 2. The SEM picture of the deposited structure morphology is shown in figure 3(c), with $P = 60$ mbar and $E = -0.55$ V. As shown in figure 3(a), the green curve represents the real-time position of the Z-axis probe, and the red curve denotes the real-time deflection of the AFP cantilever. Compared with the deflection information and the electrodeposition current of the simultaneous non-contact measurement probe [30], the measuring results obtained in this research were intuitive. More specifically, the deposition process can be directly reproduced by observing the green and red curves, and the deposition state can be effectively analyzed. Both the mechanics and current information were obtained in a single measurement [31], and force feedback identified the mechanical contact between the tip and the sample [32]. Therefore, the above two technologies provided the basis for this research.

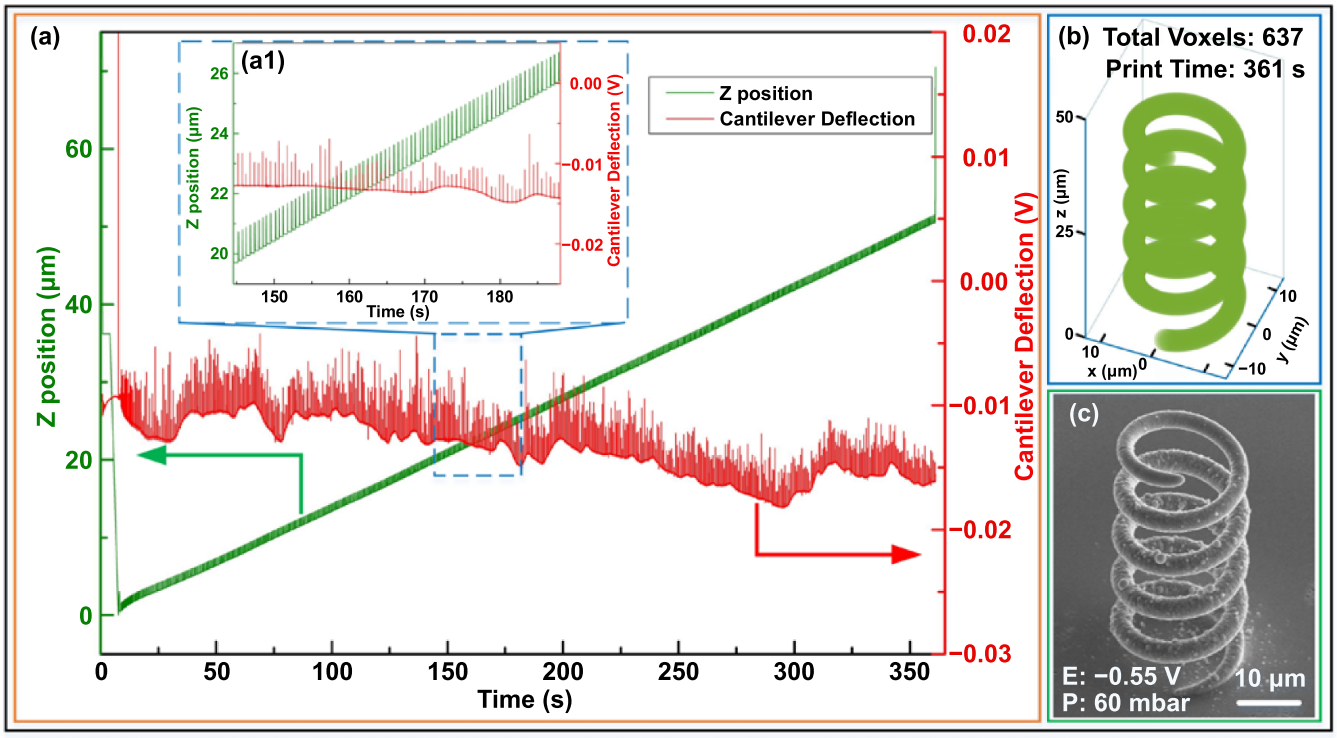

Figure 3. Simultaneous measurement of the actual position of the *Z* axis and the bending of the AFP cantilever. The blue line represents the real-time position of the *Z*-axis motor in the vertical direction, and the red line represents the cantilever deflection curve of the AFP. In the enlarged view inside, it can be clearly seen that the deposition rate in the gray shaded area is significantly higher than the subsequent deposition rate.

It can be seen that as the time (*x*-axis) increased, the position of the *Z*-axis of the green curve gradually increased and the slope remained almost unchanged. The slope of the curve represents the deposition rate of the vertical height from the top of the spring to the substrate instead of the wire length. However, the actual deposition rate of the wire structures was much higher. The actual deposition rate can be calculated from the printing time and the length of the deposition wire. As shown in figure 3(b), the micro-spiral spring deposited at this time contained a spiral structure of 637 voxels, and the total deposition time was 361 s. Theoretically, the deposition rate could be solved with Faraday's law, but it was difficult to determine its local current density. Therefore, we used the ratio of growth length to time to calculate the actual deposition rate. After calculation, the length of the helical spring wire (L) was 320.11 μm. The calculation method is shown in figure S4 in supporting information, section 2, equation (14). In summary, we obtained the helical spring wire deposition rate (v) with the following formula:

$$v = \frac{L}{t}. \tag{1}$$

The deposition rate (v) was 0.887 μm s^{-1}, and the average printing time for a voxel was about 0.567 s. The volume deposition rate (v_V) was 11.137 μm^3 s^{-1} according to supporting information, section 2, equation (15). The deposition rate was about 78.4 times greater than that of the copper wire fabricated with MCED in the evaporation state, which achieved a volume deposition rate of 0.142 μm^3 s^{-1} in the dynamic scanning mode [33].

For the same deposition file, the extrusion pressure changed in the range of 20 mbar to 70 mbar. The deposition result is shown in figure 4(a). When the extrusion pressure was $P < 50$ mbar, the deposition structure maintained the shape of the spiral spring by showing a certain gap between each coil layer. When $P \geqslant 50$ mbar, each spiral of the spring was in contact with the other spirals, forming a hollow cylinder structure. Although the spring presented a hollow cylindrical structure, surface textures were still clearly observed both inside and outside ($P = 50$ or 60 mbar). This observation may have resulted because an increase in the extrusion pressure increased the diameters of the current deposition voxels, and the enlarged voxels were in contact with the side and bottom deposition voxels at the same time, forming multidirectional deposition. However, as the extrusion pressure further increased, the surface texture of the deposit gradually disappeared and became be smooth ($P = 70$ mbar). In order to explore the influence of the surface texture on the inside of the structure, a focused ion beam (FIB) was used to mill the side of the hollow cylinder to observe its cross-sectional shape. As shown in figure 4(b), there were no macroscopic defects, such as blisters or voids, and the voxels were fused at the atomic level during the deposition process. Figures 4(c) and (d) display FIB milling graphs when the extrusion pressures were 60 mbar and 70 mbar, respectively. These two pictures fully demonstrated the high-quality deposition behavior of the LECD-μAM technology. It

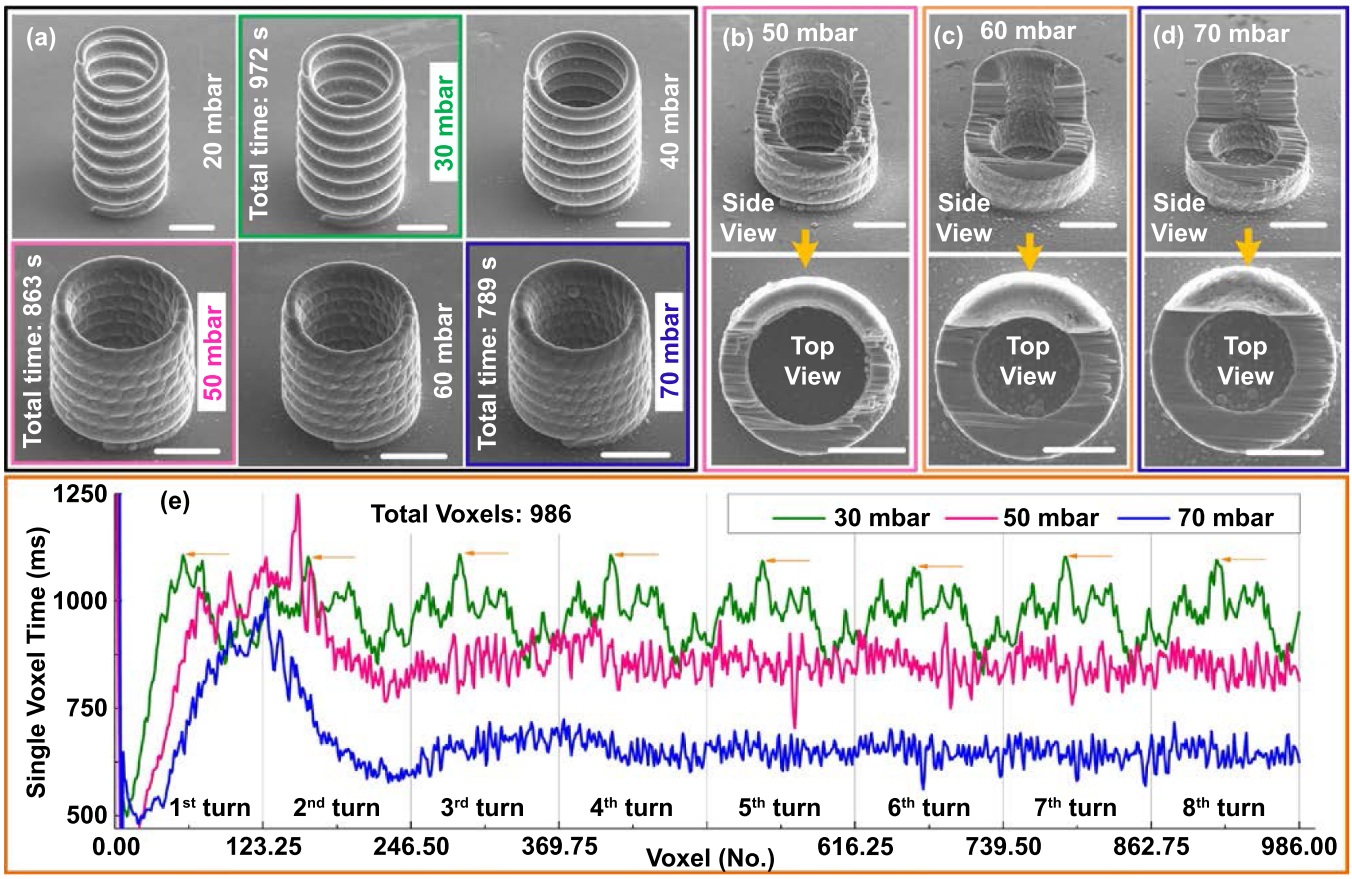

Figure 4. Print information of the deposited spiral springs. The cathode (working electrode) was applied voltage as −0.5 V, the total number of the single eight-turn close-packed spring including 986 voxels for each. (a) The morphological characteristics of the spiral microstructure under different extrusion pressures (20 mbar to 70 mbar with a 10 mbar interval) of the same printed file. (b) The side view and top view of the spiral spring milled by FIB printed in 30 mbar. (c) The side view and top view of the spiral spring milled by FIB printed in 50 mbar. (d) The side view and top view of the spiral spring milled by FIB printed in 70 mbar. (e) The deposition time of a single voxel for the whole printed period in extrusion pressure of 30 mbar, 50 mbar and 70 mbar respectively. And the 8-turn was separated by vertical lines clearly. The scale bar is equal to 10 μm in (a)–(d).

can be seen from the side view of figure 4(c) that the profile of the deposit was relatively flat, the internal material was dense, and the cross section was smooth. At the same time, as shown in the top view of figure 4(c), a few deposited particles were observed at the bottom of the hollow cylinder. This was due to the fact that a small part of the electrolyte spilled outside of the deposition area during the spraying process, generating stray deposition. For the deposition of the hollow cylindrical structure, rotating electrode LECD technology could also be useful, but a nickel tube with a diameter of up to 125 μm is required [34]. In fact, by adjusting parameters, such as the pulse potential and duty cycle, MCED could also be used to manufacture hollow cylinders with a diameter of 15 μm and a wall thickness of 1.5 μm, but the manufacturing accuracy and the outer wall surface roughness values did not meet expectations [35].

The three curves shown in figure 4(e) recorded the individual deposition time of all voxels, corresponding to the extrusion pressures of $P = 30$ mbar, 50 mbar, and 70 mbar. Figure 4(e) clearly shows that higher extrusion pressure the shortened the time required for the deposition of a single voxel. The curves at 50 mbar and 70 mbar showed roughly the same trend but at different amplitudes. The deposition time required for a single voxel was longer at $P = 50$ mbar. However, the time required for a single voxel was longest $P = 30$ mbar, as determined by its position as the top of the three curves. This was because the low extrusion pressure caused a low initial electrolyte velocity at the probe port, which reduced the convection velocity and decreased the number of metal ions reaching the deposition zone. Therefore, the time consumed to deposit a single voxel became longer. Correspondingly, for a higher extrusion pressure ($P \geqslant 50$ mbar), the structure became a hollow cylindrical structure. The increased extrusion pressure not only increased the convection velocity, but also increased the diameter of a single voxel. As a result, the contact area between the voxel and the deposited voxel increased significantly. The simultaneous contact between the side and bottom surfaces increased the access path for electric charges. According to Faraday's law, the amount of chemically changed substances on the electrode was proportional to the amount of electricity that passed through it, which increased the access path for electric charges and thereby, increased the local current density. Therefore, the deposition

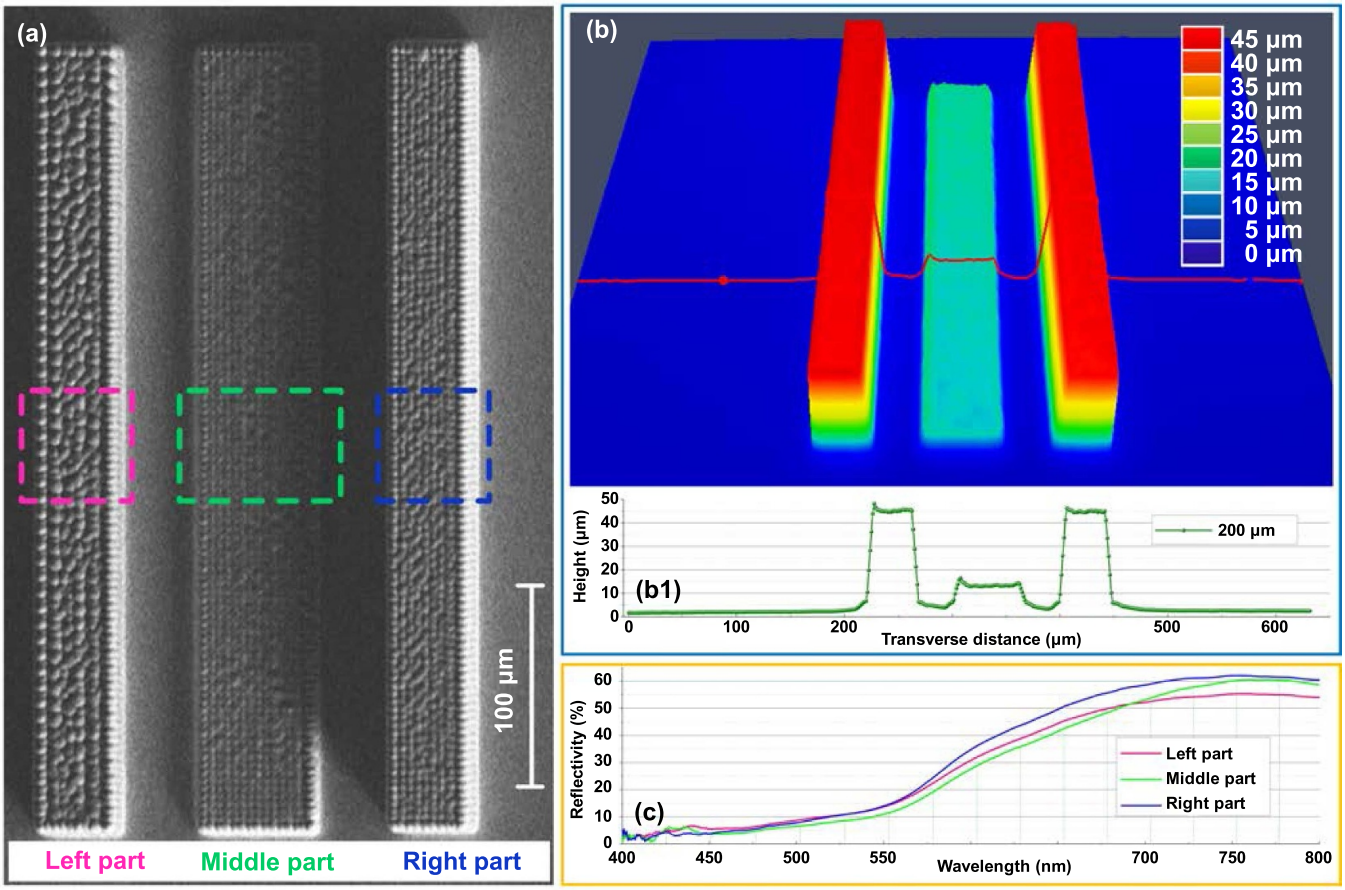

Figure 5. Large scale area three-step cuboid. (a) The SEM morphology on the top surface of the three steps. (b) The height information of the three-step cuboid. (c) The entire visible spectrum reflectivity test on three different top surfaces of the three-step cuboid.

time of a single voxel was significantly reduced. Moreover, the curve shape was significantly different from the other two curves at $P = 30$ mbar, as shown in figure 4(e). It can be clearly observed that the curve had a certain periodicity. Considering the fact that an eight-turn spring was to be deposited, we divided the X-axis into eight parts with an equal number of voxels. Except for the fact that the first coil of the foundation was slightly different, the recorded curves of the deposition times from the other seven coils showed a similar trend. It appears that the deposited spiral spring had strong repeatability for low extrusion pressure, and the intercept of each spiral point of the spring and the projection distance of the consolidation point was fixed on the substrate. This cantilever deposition characteristic was achieved by the mutual force balance between gravity and the lateral deposition of the metal atoms. In figure 4(e), the orange arrows present the longest points of the cantilever, and thus, the time was also the longest for depositing such a single voxel.

In fact, the short-time deposition process did not prove the repeatability or uniformity of the LECD-μAM technology in deposition. Therefore, we turned to a large-scale regional structure by depositing a cuboid with three steps. As shown in figure 5(a), there were some differences in the top surface morphology. Specifically, the crystals on the top surface of the left part of the steps were relatively large and a uniform micro-pit surface had formed. The top surfaces of the middle part and the right part were smoother. In order to obtain accurate height details for the deposit, a laser confocal microscope was employed to obtain the height profile of the cuboid, as shown in figure 5(b). The height details are shown in figure 5(b1). It was found that the heights of the left part and the right part were both 45 μm, and the height of the middle part was about 15 μm. Furthermore, the sides of the three steps were flat, and their steepness met the requirements. To further evaluate the influence of the top surface morphology of the three-step cuboid on the interface, an entire visible spectrum reflectivity test was carried out on its surface, as shown in figure 5(c). The three curves in the figure denote the reflectivity of different positions of the top surfaces at different steps. The results showed that the reflectivity over the entire visible spectrum did not exceed 60%. In particular, in the wavelength range of less than 550 nm, the reflectivity of the three surfaces was less than 15%. For the principle of anti-reflection, when the microstructure scale of the incident surface had the same order of magnitude as the wavelength of the light wave, the internal transmittance of the material affected the reflectivity, changing the light propagation path and increasing the degree of light absorption. Since the wavelength of the incident light was in the range of 400 nm to 800 nm, the diameter of the surface deposit was about 2.5 μm. Therefore, the diameter of the

Table 3. Chemical element composition of three different structures.

Item	Cu (%)	Si (%)	O (%)	Subtotal (%)
Micro-copper pillar	99.672	0.167	0.161	100
Hollow cylinder	99.85	0.073	0.076	100
Wall-shaped structure	99.595	0.072	0.332	100

deposited particles on the surface of the deposited body had almost the same order of magnitude as the wavelength of the incident light, thus increasing the absorption of light. Fortunately, we found that although the morphology was slightly different, the interface did not significantly influence the light reflection performance. This was very important for printing consistency and maintaining the accuracy of the continuous printing process.

3.2. Chemical element in deposit

Next, the chemical composition in the deposit manufactured with LECD-μAM technology was further explored. A JEOL JXA-8530F Plus field emission electron probe microanalyzer with the x-ray spectrum was used to measure the chemical composition of the deposit. The measurement results are shown in table 3. The content of metallic copper in all of the deposits exceeded 99.5%, achieving almost pure copper AM. The individual test results for each structure are shown in figure S5 (supporting information, section 3). The results show that the copper content was much higher than that in the preparation of suppressed oxide [36]. The same was true for the oxidation-resistant copper nanowire manufacturing process, and the deposition results proved the existence of carbon [37].

It could be seen from the above results that using hollow AFPs for deposition in the supporting solution prevented the chemical elements in the air from influencing the deposits. In the LECD-μAM process, including the metal salt solution and the supporting solution, the cations were only copper ions and hydrogen ions, so other metal elements were not reduced at the WE. Hydroxide oxidized at the CE to generate oxygen, which was also the main reason the chemical composition contained oxygen. The main impact occurred after deposition, and it was unavoidable that the sample was in contact with the air during transportation. If the LECD-μAM structure was transferred to an x-ray spectrometer in an oxygen-free environment, the oxygen content would have been less than that in the above result. In addition, it is necessary to explain the source of silicon. Since all of the deposition experiments were carried out on a wafer substrate, each structure contained a small amount of silicon. Therefore, it was concluded that we had confidence in achieving a nearly pure metal preparation process with LECD-μAM technology and that these pure copper metal structures were expected to have great potential in signal and data transmission.

3.3. Mechanical properties

In order to further explore the basic characteristics of the LECD-μAM-printed structures, the mechanical properties of a five-turn micro-spring were analyzed. As shown in figure 6(a), a punch with a diameter of 200 μm was used to perform compression tests on tiny springs. Figure 6(b) shows the force-position curves of the springs under different extrusion pressures. With the same applied voltage, an increase in the extrusion pressure inevitably led to an increased diameter of the spring wire, as shown in figure S7 (supporting information, section 4, figure S7). Additionally, the increasing diameter caused the slope of the curve in figure 6(b) to increase significantly, and hence, the coil spring stiffness (c_{spring}) also increased (supporting information, section 4, table S1). The reason for this was that the increase in the diameter of the deposited spring wire enhanced the ability of the spring to resist deformation, and thus, the spring stiffness increased accordingly. c_{spring} was obtained from the data in the middle stable stage of the force–displacement curve shown in figure 6(b). According to the calculation formula of the spring stiffness, the shear modulus (G) of the spring material was deduced. The formula is as follows:

$$c_{\text{spring}} = \frac{F_{\text{load}}}{l} = \frac{G \times {d_1}^4}{8 \times D_1^3 \times n_1} \tag{2}$$

where F_{load} represents the load on the spring, l is the deformation of the spring under load F_{load}, d_1 represents the diameter of the spring wire, 2.51 μm (corresponding to the extrusion pressure of 60 mbar), D_1 is the spring diameter, 40 μm, c_{spring} is equal to 9.425 N m^{-1}, and n_1 is the effective turn number of the springs.

The whole experiment process is shown in supporting information, movie 1. The shear modulus of the helical spring material was about 60.8 GPa based on the formula, much higher than that of bulk copper (~44.2 GPa). The reason for the high shear modulus was that the deposit had a micron-level size. The single-crystal grain structure was not generated for the condition of local high current density, and the crystal grain size had to be at the nanometer level. As a result, a high shear modulus was produced. Although the mechanical test methods were different, the previous results also showed extremely high strength characteristics. The yield strength of the copper wire, which was 1.5 μm in diameter, reached 317 MPa [38], and the yield strength of the copper microstructure with nanocrystalline-nanotwinned crystals exceeded 960 MPa [39].

3.4. Printing of microstructures

The AM of complex/array microstructures can be achieved using LECD-μAM technology. This technology has high manufacturing precision, good quality, high deposition rates, and high repeat positioning accuracy. The manufacturable structure does not require masks or cantilevers, and there is a

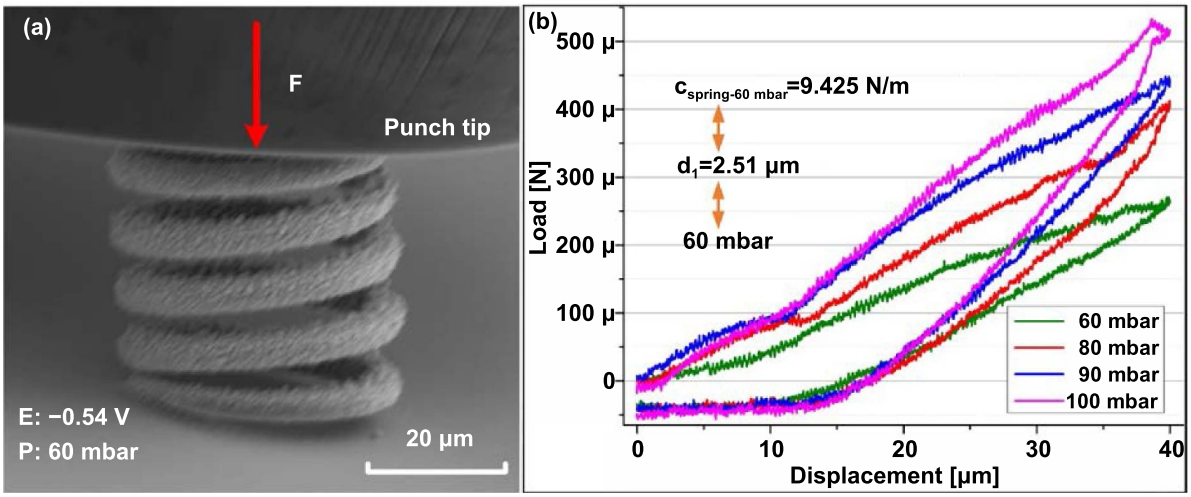

Figure 6. Mechanical performance analysis of printed microscale springs. (a) The force of the spring structure deposited by localized electrochemical deposition; (b) the spring stiffness of four springs deposited by different deposition pressures were tested.

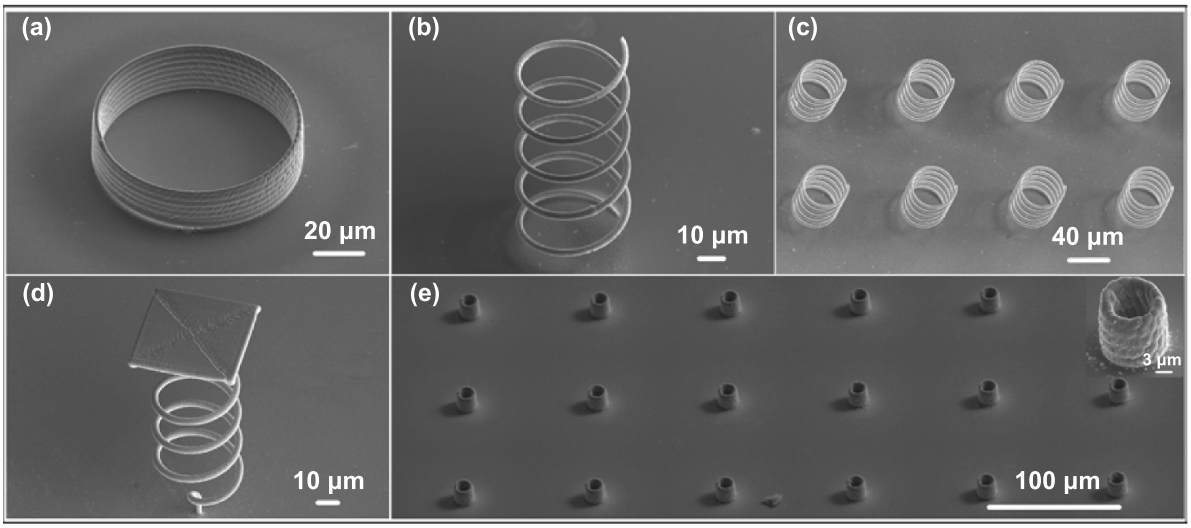

Figure 7. Different tiny structures designed and manufactured based on the main body of the spring structure. (a) Larger hollow tube, (b) a single five coil spring, (c) three array micro-spring structure, (d) a single spiral flat-top structure, (e) a tiny hollow cylinder formed by close-packed springs array.

high aspect ratio. Furthermore, this technology is suitable for many types of structures, including micro-cylinders, hollow cylinders, flat-top springs, spring arrays, and hollow cylinder arrays. The results after using LECD-μAM micro-deposition to fabricate metal micro-pillars for the parametric experiments are displayed in figures S6 and S7 (supporting information, section 4). It was found that the smallest deposition wire diameter reached about 800 nm when −0.56 V voltage was applied to the substrate at $P = 10$ mbar using a 300 nm opening tip. As shown in figure 7, the voltages chosen for the deposition ranged between −0.46 V and −0.56 V. Figure 7 shows the different microstructures designed and manufactured based on the main body of the spring structure. Figure 7(a) shows a hollow tube with a larger diameter, figure 7(b) displays a high-quality five-coil spring, figure 7(c) illustrates a five-coil spring array structure, figure 7(d) shows a single flat-topped coil spring support structure, and figure 7(e) shows an array of tiny hollow cylinders formed by tightly packed coil springs. Therefore, LECD-μAM technology was proven an effective method to fabricate these high-quality structures.

4. Conclusions

In this work, LECD-μAM technology with atomic force servo closed-loop control was used to manufacture tiny pure copper structures in a single step. Firstly, by simultaneously monitoring the Z-axis coordinates and the deflection of the AFP cantilever, the deposition voxel moved automatically to the next position for deposition after formation. The entire process was automatic and efficient. Secondly, the deposition experiment was carried out using the same print file and varying the applied pressure from 20 to 70 mbar. The wire diameter of the deposited micro-helical structure also changed, as determined

through SEM image analysis. When the spring wire was close enough, the structure formed a hollow cylinder. The results of the deposition experiment suggest that the extrusion pressure had a close relationship with the deposition time of a single voxel. As the extrusion pressure increased, the time it took to deposit a single voxel gradually decreased. Furthermore, the field emission electron probe spectrometer was used to test the chemical composition of the deposited structures. The experimental results of the LECD-μAM based on the AFP technology and the copper content, which exceeded 99.5%, proved that the deposited structure was an almost pure metal printing. Finally, the *in-situ* nanoindenter integrated in the field emission electron microscope was used to test the stiffness of the deposited spring, and the shear modulus of the copper spring structure was calculated. The obtained shear modulus value was significantly higher than that of the bulk copper material. By changing and combining different spring structures, the manufacture of the hollow ring structures, micro-springs, micro-spring array structures, springs with flat top, and hollow cylindrical large-area array structures was achieved. Although LECD-μAM technology can be used to manufacture pure copper microchip bridges, micro-antennas, micro-sensors, and other small structures without masks and supporting materials, the technology still has a low deposition rate and is prone to a probe clogging problem. The next step of the research is to introduce a parallel manufacturing method for multiple probes to increase the deposition rate while applying a reverse voltage to avoid probe clogging.

Acknowledgments

This work was supported by the National Natural Science Foundation of China under Grant U19A20103; and the Fund for Jilin Province Scientific and Technological Development Program under No. Z20190101005JH.

ORCID iD

Jinkai Xu https://orcid.org/0000-0002-5373-4564

References

[1] Richner P, Eghlidi H, Kress S J P, Schmid M, Norris D J and Poulikakos D 2016 Printable nanoscopic metamaterial absorbers and images with diffraction-limited resolution *ACS Appl. Mater. Interfaces* **8** 11690–7

[2] Sundaram M, Kamaraj A B and Lillie G 2018 Experimental study of localized electrochemical deposition of Ni-Cu alloy using a moving anode *Proc. CIRP* **68** 227–31

[3] Farahani R D, Chizari K and Therriault D 2014 Three-dimensional printing of freeform helical microstructures: a review *Nanoscale* **6** 10470–85

[4] Farahani R D, Dalir H, Le Borgne V, Gautier L A, El Khakani M, Lévesque M and Therriault D 2012 Direct-write fabrication of freestanding nanocomposite strain sensors *Nanotechnology* **23** 085502

[5] Ahn B Y, Duoss E B, Motala M J, Guo X Y, Park S-I, Xiong Y J, Yoon J, Nuzzo R G, Rogers J A and Lewis J A 2009 Omnidirectional printing of flexible, stretchable, and spanning silver microelectrodes *Science* **323** 1590–3

[6] Skylar-Scott M A, Gunasekaran S and Lewis J A 2016 Laser-assisted direct ink writing of planar and 3D metal architectures *Proc. Natl Acad. Sci. USA* **113** 6137–42

[7] Feinaeugle M, Pohl R, Bor T, Vaneker T and Römer G W 2018 Printing of complex free-standing microstructures via laser-induced forward transfer (LIFT) of pure metal thin films *Addit. Manuf.* **24** 391–9

[8] Miikkulainen V, Leskelä M, Ritala M and Puurunen R L 2013 Crystallinity of inorganic films grown by atomic layer deposition: overview and general trends *J. Appl. Phys.* **113** 021301

[9] George S M 2010 Atomic layer deposition: an overview *Chem. Rev.* **110** 111–31

[10] Wang M, Huang Z, Salut R, Suarez M A, Lu H H, Martin N and Grosjean T 2021 Plasmonic helical nanoantenna as a converter between longitudinal fields and circularly polarized waves *Nano Lett.* **21** 3410–7

[11] Madden J D and Hunter I W 1996 Three-dimensional microfabrication by localized electrochemical deposition *J. Microelectromech. Syst.* **5** 24–32

[12] Ciou Y J, Hwang Y R and Lin J C 2015 Theoretical modeling and fabrication of two-dimensional microstructures by using micro-anode-guided electroplating with real-time image processing *Key Eng. Mater.* **656–657** 604–14

[13] Lin J C, Chang T K, Yang J H, Chen Y S and Chuang C L 2010 Localized electrochemical deposition of micrometer copper columns by pulse plating *Electrochim. Acta* **55** 1888–94

[14] Brant A and Sundaram M 2016 A novel electrochemical micro additive manufacturing method of overhanging metal parts without reliance on support structures *Proc. Manuf.* **5** 928–43

[15] Xu J K, Ren W F, Lian Z X, Yu P and Yu H D 2020 A review: development of the maskless localized electrochemical deposition technology *Int. J. Adv. Manuf. Technol.* **110** 1731–57

[16] Zhao M, Du L, Wei Z, Du C, Liu X and Ji X 2018 Fabrication of metal microfluidic chip mold with coplanar auxiliary cathode in the electroforming process *J. Micromech. Microeng.* **29** 025002

[17] Sundaram M, Drexelius A and Kamaraj A B 2019 A study on the effect of interelectrode gap in the electrochemical additive manufacturing process *Mach. Sci. Technol.* **23** 232–48

[18] Wang F, Bian H and Xiao Y 2019 Fabrication of micro-sized copper columns using localized electrochemical deposition with a 20 μm diameter micro anode *ECS J. Solid State Sci. Technol.* **8** 223–7

[19] Kamaraj A B and Sundaram M 2019 A mathematical model of the deposition rate and layer height during electrochemical additive manufacturing *Int. J. Adv. Manuf. Technol.* **102** 2367–74

[20] Behroozfar A, Daryadel S, Morsali S R, Moreno S, Baniasadi M, Bernal R A and MinaryaJolandan M 2017 Microscale 3D printing of nanotwinned copper *Adv. Mater.* **30** 1705107

[21] Lin Y-P, Zhang Y and Yu M-F 2018 Parallel process 3D metal microprinting *Adv. Mater. Technol.* **4** 1800393

[22] Ciou Y-J, Hwang Y-R, Lin J-C and Tseng Y-T 2016 Fabrication of 3D microstructure by localized electrochemical deposition with image feedback distance control and five-axis motion platform *ECS J. Solid State Sci. Technol.* **5** 425–32

[23] Hu J and Yu M-F 2010 Meniscus-confined three-dimensional electrodeposition for direct writing of wire bonds *Science* **329** 313–6

[24] Dermutz H, Grüter R R, Truong A M, Demkó L, Vörös J and Zambelli T 2014 Local polymer replacement for neuron

patterning and *in situ* neurite guidance *Langmuir* **30** 7037–46
[25] Meister A *et al* 2009 FluidFM: combining atomic force microscopy and nanofluidics in a universal liquid delivery system for single cell applications and beyond *Nano Lett.* **9** 2501–7
[26] Meister A *et al* 2009 Nanoscale dispensing in liquid environment of streptavidin on a biotin-functionalized surface using hollow atomic force microscopy probes *Microelectron. Eng.* **86** 1481–4
[27] Hirt L, Ihle S, Pan Z J, Dorwling-Carter L, Reiser A, Wheeler J M, Spolenak R, Vörös J and Zambelli T 2016 Template-free 3D microprinting of metals using a force-controlled nanopipette for layer-by-layer electrodeposition *Adv. Mater.* **28** 2311–5
[28] Hirt L, Grüter R R, Berthelot T, Cornut R, Vörös J and Zambelli T 2015 Local surface modification *via* confined electrochemical deposition with FluidFM *RSC Adv.* **5** 84517–22
[29] Zhao J L, Swartz L A, Lin W-F, Schlenoff P S, Frommer J, Schlenoff J B and Liu G-Y 2016 Three-dimensional nanoprinting *via* scanning probe lithography-delivered layer-by-layer deposition *ACS Nano* **10** 5656–62
[30] Geerlings J, Sarajlic E, Berenschot E J W, Sanders R G P, Siekman M H, Abelmann L and Tas N R 2015 *Appl. Phys. Lett.* **107** 123109
[31] Ossola D, Dorwling-Carter L, Dermutz H, Behr P, Vörös J and Zambelli T 2015 Simultaneous scanning ion conductance microscopy and atomic force microscopy with microchanneled cantilevers *Phys. Rev. Lett.* **115** 238103
[32] Dorwling-Carter L, Aramesh M, Forró C, Tiefenauer R F, Shorubalko I, Vörös J and Zambelli T 2018 Simultaneous scanning ion conductance and atomic force microscopy with a nanopore: effect of the aperture edge on the ion current images *J. Appl. Phys.* **124** 174902
[33] Lei Y, Zhang X, Xu D, Yu M, Yi Z, Li Z, Sun A, Xu G, Cui P and Guo J 2018 Dynamic "scanning-mode" meniscus confined electrodepositing and micropatterning of individually addressable ultraconductive copper line arrays *J. Phys. Chem. Lett.* **9** 2380–7
[34] Yeo S H and Choo J H 2001 Effects of rotor electrode in the fabrication of high aspect ratio microstructures by localized electrochemical deposition *J. Micromech. Microeng.* **11** 435
[35] Seol S K, Kim D, Lee S, Kim J H, Chang W S and Kim J T 2015 Electrodeposition-based 3D printing of metallic microarchitectures with controlled internal structures *Small* **11** 3896–902
[36] Yi Z R, Lei Y, Zhang X Y, Chen Y N, Guo J J, Xu G J, Yu M-F and Cui P 2017 Ultralow flexural properties of copper microhelices fabricated *via* electrodeposition-based three-dimensional direct-writing technology *Nanoscale* **9** 12524–32
[37] Yi Z R, Guo J J, Chen Y N, Zhang H Q, Zhang S, Xu G J, Yu M F and Cui P 2016 Vertical, capacitive microelectromechanical switches produced via direct writing of copper wires *Microsyst. Nanoeng.* **2** 16010
[38] Eliyahu D, Gileadi E, Galun E and Eliaz N 2020 Atomic force microscope-based meniscus-confined three-dimensional electrodeposition *Adv. Mater. Technol.* **5** 1900827
[39] Daryadel S, Behroozfar A, Morsali S R, Moreno S, Baniasadi M, Bykova J, Bernal R A and Minary-Jolandan M 2017 Localized pulsed electrodeposition process for three-dimensional printing of nanotwinned metallic nanostructures *Nano Lett.* **18** 208–14